



TECHNICAL ARTICLE

# Dilatometric and Microstructural Investigations on Austenite Decomposition under Continuous Cooling Conditions in a Cu-Bearing High-Strength Low-Alloy Steel

Atul Kumar, Lambodar Sahoo, Deepak Kumar, Vajinder Singh, K. Gopinath, and R. Balamuralikrishnan

Submitted: 31 October 2021 / Accepted: 16 April 2022 / Published online: 18 May 2022

High-strength low-alloy (HSLA) steels are an important class of steels that meet combinations of varied properties demanded by critical engineering applications. Microstructures of this class of steels are engineered to meet the targeted mechanical properties. Thorough understanding of phases that evolve during decomposition of austenite in these steels after hot working or after austenitizing treatments is essential to optimize their key processing parameters. This is achieved through establishment of continuous cooling transformation diagrams. These diagrams shed light on details of cooling transformations like the phases formed during transformation, sequence of transformation when multiple phase transformations are involved and the temperatures at which the transformations start and end, all as a function of cooling rate. These diagrams are constructed from dilatometry experiments together with corroborating microstructural investigations and mechanical property assessments. However, analyses of dilatograms, identification and quantification of microstructural constituents and correlating the same with mechanical properties (usually hardness) are not trivial, especially, in low-carbon HSLA steels where the microstructure is often composed of martensite and bainite that have rather similar morphological features and practically difficult to distinguish from each other. Advanced data processing of electron backscattered diffraction (EBSD) data has been used in recent times with considerable success to differentiate bainite and martensite. This work highlights the salient aspects involved in decomposition of austenite in an indigenously developed Cu-bearing HSLA steel. Details of methodology employing grain average misorientation obtained through EBSD experiments to identify and quantify martensite and bainite are discussed in detail.

**Keywords** CCT, dilatometry, grain average misorientation, gleeble, HSLA

## 1. Introduction

Materials for structural applications in naval vessels should have reasonably high strength, good resistance to fatigue and various forms of corrosion, and excellent impact toughness down to temperatures as low as  $-60\text{ }^{\circ}\text{C}$ . It is also necessary that the material has adequate formability and excellent weldability. These demands have led to the development of high-strength low-alloy (HSLA) steels, which are micro-alloyed steels better than conventional carbon steels in respect of the above demands. They contain very low-carbon levels, and contain substitutional alloying elements, such as manganese, nickel, chromium and molybdenum for hardenability and copper for precipitation hardening (Ref 1). HSLA steels are not considered to be alloy steels in the normal sense because they are designed to meet specific mechanical properties rather than a chemical composition (Ref 2). HSLA steels of varying strength levels

find main application in oil and gas pipelines, bridges, offshore structures and naval vessels. Depending on the property requirements dictated by the application, yield strength levels of HSLA steels range from 275 to 1100 MPa (Ref 3, 4). Such a range in mechanical property levels are achieved in HSLA steels through tailoring of microstructural constituents which could range from pearlitic to acicular ferritic (Ref 5) to ferrite + pearlite to ferrite + martensite/bainite (Ref 6) to tempered martensite/bainite, etc. (Ref 7).

After gaining expertise of developing relatively lower strengths (up to  $\sim 600\text{ MPa}$ ), low-carbon HSLA steels in the past (Ref 8), a new copper bearing HSLA steel has been produced targeting minimum room temperature yield strength of 780 MPa together with a minimum Charpy V-notch impact toughness of 78 J at  $-40\text{ }^{\circ}\text{C}$  (Ref 9, 10). The steel developed has been produced in limited quantities on an industrial scale successfully meeting the targeted properties, largely relying on the past experience in processing similar class of steels. However, a thorough understanding of phase transformations involved in the steel is yet to be developed. Ability to tailor its microstructures to meet targeted mechanical properties in a robust manner calls for a thorough understanding of the physical metallurgical aspects of the steel especially phase transformations and transformation products. More importantly, knowledge of transformation products under industrial continuous cooling conditions is of importance to understand phases present in it and to optimize the heat treatments accordingly to meet the targeted combination of properties. For the studied

Atul Kumar, Lambodar Sahoo, Deepak Kumar, Vajinder Singh, K. Gopinath, and R. Balamuralikrishnan, Defence Metallurgical Research Laboratory, Kanchanbagh, Hyderabad 500058, India. Contact e-mails: atulmbg.dmr@gmail.com; atul.dmr@gov.in.

class of steel, after austenitization during cooling, the austenite decomposes to different low-temperature phases/aggregates, viz., ferrite, pearlite, bainite and martensite or a mixture of these phases depending on the cooling rate adopted. Specimens cooled from austenitic regime at different controlled cooling rates undergo volume changes depending on the transformation products generated. The associated change in its linear dimension can be accurately captured through a dilatometer as a function of temperature. Dilatograms generated as a function of cooling rate can be analyzed to track start, progress and end-of-phase transformations (Ref 11). The constituents of the resulting microstructure are assessed through standard metallographic techniques and correlated with hardness measurements made on cooled sections. The results are presented typically in the form of continuous cooling transformation (CCT) diagrams showing the envelope of start and end of transformations as a function of cooling rate together with the details of transformation products and their hardness levels.

The steel studied in this particular work belongs to a class of low-carbon low-alloy steel. Whenever multiple low-temperature phases (such as bainite, martensite and ferrite) are possible, as in our case, it is important to identify them. In the literature, the conventional metallographic approaches for distinguishing multiple low-temperature phases are given mainly for medium- or high-carbon steels, but rarely for low-carbon low-alloy steels, as unambiguous identification of the phases is impossible in such steels. Nevertheless, a clear identification of the different phases is crucial in establishing an accurate CCT diagram. Toward reliable identification of phases, a promising EBSD-based technique to delineate the various low-temperature phases in low-carbon low-alloy steels has emerged in recent times. This indirect technique, pioneered by Zisman and co-workers (Ref 12, 13), utilizes the expected variation in dislocation densities between the different phases, which manifests in the measure of grain average misorientation (GAM). While Zisman and co-workers have illustrated the potential of this technique for identifying the phase constituents at selected cooling rates, we have adopted this approach across multiple cooling rates spanning from 0.05 to 50 °C/s systematically. This novel approach has helped us not only in delineating the phases essential for generating CCT diagram but also in quantifying their fractions.

## 2. Experimental

### 2.1 Material

The steel under study, designated HSS1, was melted and continuously cast in an industrial scale. A 50 Ton vacuum melted heat was produced through electric arc melting followed by ladle refining and vacuum degassing. The steel was cast into slabs of dimensions 2800 mm × 900 mm × 250 mm through

continuous casting route. The chemical composition of steel under study is shown in Table 1.

Rolling of the slab into plates of various thickness and heat treatment of the plates were also carried out at an industrial scale. Prior to rolling, slabs were soaked at a temperature in the range of 1200-1240 °C. Carefully designed industrial rolling schedules were employed to achieve the final plate thickness ranging from 30mm to 70mm. The material for the present study was extracted from a plate with supply dimensions 7000 mm × 2000 mm × 30 mm with a finishing rolling temperature of approximately 850-950 °C. While approximately 8-12% reduction was given during the initial 10 passes, for remaining passes higher deformation up to 15-20% per pass was adopted. After rolling, plates were air-cooled to room temperature. Heat treatment involving hardening and tempering treatments was carried out on the rolled plate to achieve the targeted mechanical properties (YS > 780 MPa, UTS > 850 MPa, % El > 13, a sub-zero Charpy impact toughness ≥ 78J at -40 °C). Hardening was carried out at 900 °C for 2 h followed by water quenching to room temperature. Subsequently, tempering was carried out at 610 °C for 3 hours followed by water quenching to room temperature. The optical micrograph of the steel in the hardened and tempered condition revealing tempered martensitic structure is shown in Fig. 1.

### 2.2 Dilatometry

The geometry of the specimen used to conduct dilatometry experiments in Gleeble is shown at Fig. 2, which is as per ASTM standard A1033-10. Temperature of the reduced section used for dilatometry is measured and controlled through K-type thermocouple wires (Chromel/Alumel), of diameter 0.02 mm, spot welded to the specimen at the mid span perpendicular to the sample axis. Both the wires were spot welded at 32V. During the experiments, samples were heated to austenitization temperature of 925 °C (Ref 9) at a heating rate of 5 °C/sec and held at that temperature for 1 minute. The samples were then cooled from 925 °C to room temperature at six different cooling rates of 0.05, 0.2, 0.5, 1, 10 and 50 °C/sec. Cooling rates for this study were selected based on the cooling rates adopted in

**Table 1** Nominal composition of the steel studied (wt.%)

C	Si	Mn	Ni+Cu	Cr + Mo
0.05-0.10	0.2-0.3	0.8-1.4	4-6	0.4-1.5

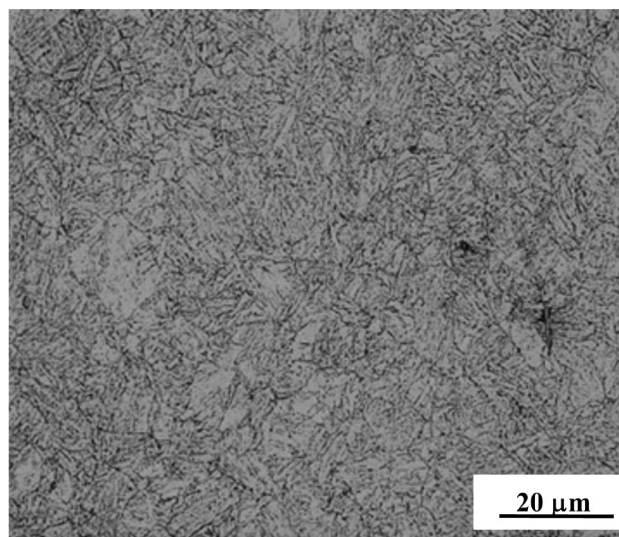


**Fig. 1** Microstructure in the as-received condition revealing tempered martensitic structure

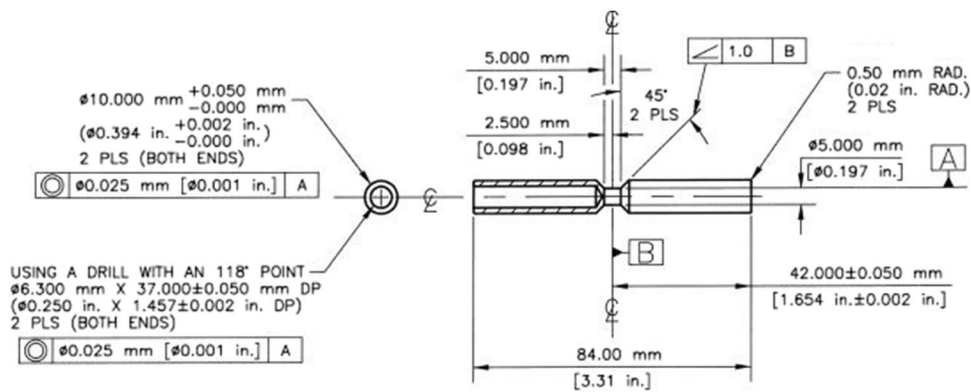


Fig. 2 Specimen dimension for dilatometry experiments in Gleeble

studies published earlier for this class of steels, *viz.* HSLA 80, HSLA 100 (Ref 14, 15).

### 2.3 Hardness Measurements

After the dilatometry tests, the specimens were cut at the mid-point (where thermocouple wires were welded) and one half of the specimen was prepared for hardness measurements. Hardness testing was carried out using a micro Vickers hardness tester (SSS Instruments, Pune) with an applied load of 30 Kgf and a dwell time of 10 sec. As the control thermocouple is located at the middle of the specimen (and for specimen heated in Gleeble, temperature is uniform across the specimen thickness), all hardness measurements were carried out on the mid-transverse section of the specimen. For each specimen pertaining to a specific cooling rate, three hardness measurements were carried out and an average hardness value is reported with error bars.

### 2.4 Microstructural Characterization

The specimens were cut along the mid-transverse section and then mounted and metallographically polished. The polished samples were etched with 2% Nital to characterize the microstructure. The optical micrographs were captured using optical microscope (Olympus) at different magnifications. Scanning electron microscopic (SEM) examinations of the specimens were carried out on FEI Quanta 400 SEM at 20 kV acceleration voltage. The electron backscattered diffraction (EBSD) analyses were carried out in a Zeiss FEGSEM Supra55 attached with Oxford Nordlys EBSD detector and data analysis were performed using TSL 8.0 software. In order to select an area for the EBSD GAM analysis, initially, SEM micrographs were taken at a lower magnification from different regions of the specimen. Subsequently, the same areas were also examined at higher magnifications in order to ensure that microstructure is uniform. One such region at the chosen magnification was selected for performing EBSD GAM analysis. EBSD scans were performed with the step size of  $0.225\ \mu\text{m}$  at  $2500\times$  magnification. Grain average misorientation (GAM) data, which is obtained from the raw EBSD data, was used as the main parameter to delineate subtle differences among the non-FCC constituents *viz.* bainite and martensite. GAM analysis is available as a standard part of the TSL 8.0 software. The details of EBSD analyses are elaborated in Sect. 3.5.2(b).

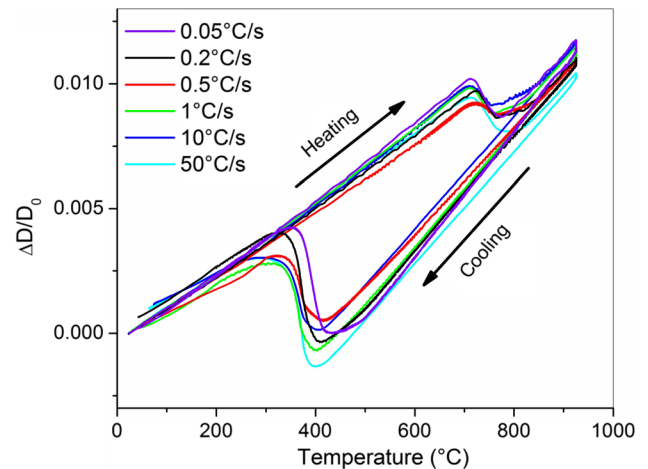


Fig. 3 Dilation data captured as a function of temperature during heating and cooling of dilatometry specimens

## 3. Results and Discussion

The steel being studied was developed through modifications to the composition of an established and productionized 600 MPa class steel (DMR249B) through thermodynamic calculations and published knowledge on HSLA steels like HSLA 80 and 100. Hence, it is expected that there would be many similarities with other quenched and tempered steels in terms of its microstructure and other physical metallurgical characteristics. The characteristics of austenite decomposition exhibited by the steel during continuous cooling at different cooling rates captured through dilatometry are presented in following sections together with hardness and supporting microscopy.

### 3.1 Heating and Cooling Transformations

Dilatation data on the specimens were captured as a function of temperature during heating (at  $5\ \text{°C/sec}$  in all tests) to an austenitization temperature of  $925\ \text{°C}$  and cooling from there at six different cooling rates in the range of  $0.05\text{--}50\ \text{°C/sec}$  (see Fig. 3). From the heating segments of the dilatation curves in Fig. 3, a major phase transformation involving reduction in volume is noticed at about  $700\ \text{°C}$ . This represents the transformation to austenite; the start ( $A_{c1}$ ) and end ( $A_{c3}$ ) of the transformation to austenite were determined to be  $698 \pm 13$

°C and  $765 \pm 7$  °C, respectively, using lever-rule method (Ref 16). Unlike  $Ac_1$  and  $Ac_3$  temperatures that are same in all tests, as they are captured from heating curves, which were all at 5 °C/s, cooling transformation temperatures captured from cooling curves are known to vary with cooling rate as the transformation products and the nature of transformation vary with cooling rate. Start of a transformation can be clearly spotted from the deviation in linearity of the cooling curves at around 400-500 °C. Similarly an end of a transformation can be picked up at around 200-300 °C below which the cooling curves start to exhibit linearity again on cooling. While an overall volume increase is clear between the two linear cooling segments, closer examination of the segment of the cooling curve between the two linear segments revealed minor slope changes indicative of the potential presence of more than one transformation. This is not uncommon as steels are known to exhibit multiple phase transformations upon cooling from austenite at certain cooling rates. However, identification of the start and end points of such transformations from the dilatation curves is difficult by conventional line deviation methods as the slope changes are minor and not easily noticeable. The cooling curves can be further complicated by the precipitation of various phases within the austenitic or the ferritic matrix.

Although the cooling curves show indications of more than one transformation, the two major transformation points were first estimated through lever-rule method (Ref 16), which ignores the presence of any additional transformations in between. To define other transformation points present in

between the major transformation points, first and second derivatives of the cooling curves were employed. This is illustrated in Fig. 4 using the cooling curve pertaining to 10 °C/sec as an example. While Fig. 4(a) shows the full cooling curve, Fig. 4(b) shows the portion of the cooling curve selected for determination of transformation points. Figure 4(c) and (d) shows the first and second derivatives of the selected segment of the cooling curve with identical x-axes as that of Fig. 4(b). Taking clues from the manifestations of the subtle slope changes in dilatation curves on their first and second derivatives, start and end points of two transformations could be identified as indicated by the vertical dotted and dashed lines. The identified transformation points are marked as 1, 2, 3 and 4 for illustration in Fig. 5 on the corresponding cooling curve pertaining to 10 °C/s. Similar exercise was carried out for all the cooling curves to identify the transformation points. In all the cases, the two major transformation points identified through phase fraction approach matched very well with the first and last transformation points identified through use of derivatives. Four transformation points could be identified at all cooling rates except the slowest cooling rate of 0.05 °C/s where only two transformation points could be identified. Boundaries demarking the transformed phases are generated by joining all the transformation points corresponding to 1st, 2nd, 3rd and 4th transformations (Fig. 5). However, identifying the phases involved in transformations at different cooling rates requires assessment of the resultant microstructures and their hardness as discussed in the subsequent sections.

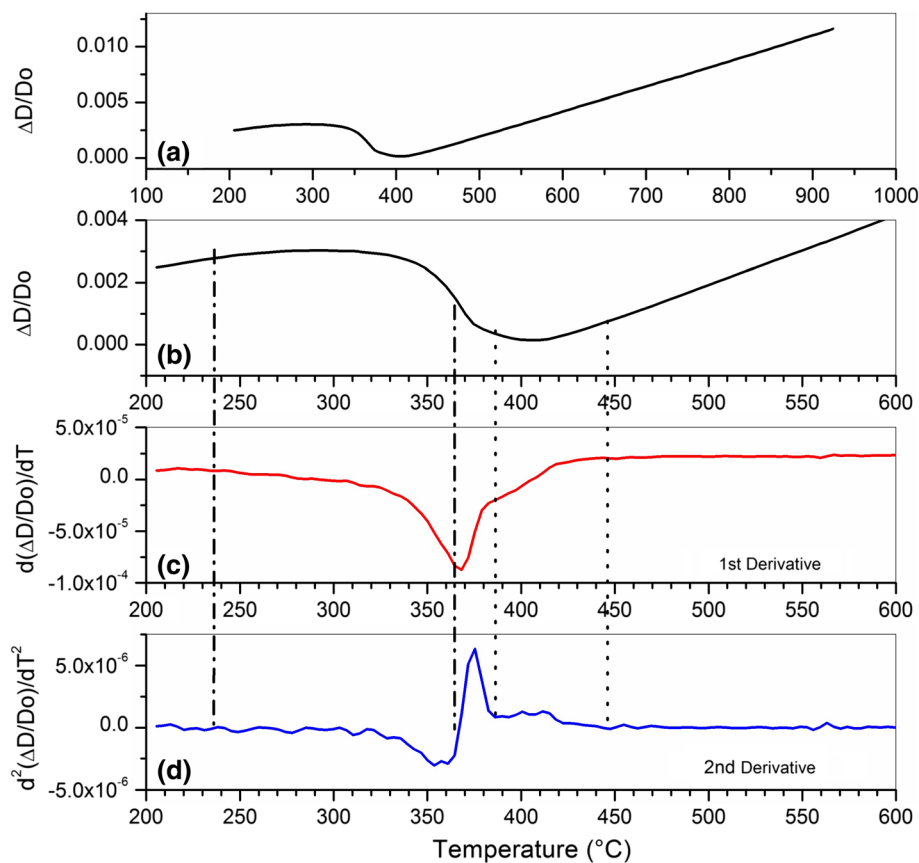


**Fig. 4** Procedure for analyzing the obtained dilatometry data for determining critical transformation temperature for cooling rate 10 °C/sec

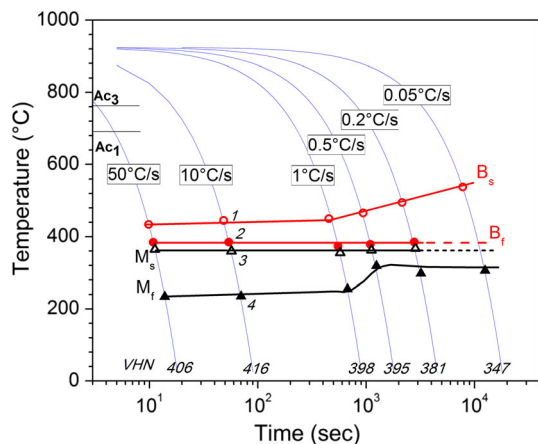


Fig. 5 CCT diagram for the steel under study

### 3.2 Hardness

The individual hardness values (i.e., an average of three values determined) on any given section did not vary by more than 9 VHN in any of the specimens. These hardness values are quite accurate representation of hardness pertinent to the corresponding microstructure dictated by the cooling rate. The Vickers hardness of the investigated steel HSS1 is also shown in Fig. 5 for different cooling rates (0.05-50 °C/sec). The hardness values are also plotted against cooling rate in Fig. 6. The most marked increase in hardness is seen when the cooling rate is increased from 0.05 °C/sec to 1 °C/sec (from 347 to 398 VHN), but thereafter the increase is gradual, reaching up to a maximum of 416 VHN. Further, the overall increase in hardness is only about 20% (Min: 347 VHN to Max: 416 VHN) even when the cooling rates increase by three orders of magnitude (i.e., 0.05-50 °C/sec). Such rather marginal increase in hardness with cooling rate is an indication that the constituents of the microstructures resulting from different cooling rates are not significantly different. The details of microstructure will be discussed in the following sections.

### 3.3 Optical and Scanning Electron Metallography

The optical micrographs of specimens cooled at different cooling rates are also shown in Fig. 6 together with the plot of variation in hardness with cooling rate. The observations on optical micrographs described below are based on inferences made from careful scrutiny of multiple microstructures at every cooling rate at various larger magnifications than presented in Fig. 6. It can be said that barring the microstructure at the slowest cooling rate of 0.05 °C/sec, microstructural features of all other cooling rates have many similarities to varying extents depending on the cooling rate. In the micrograph pertaining to 0.05 °C/sec (Fig. 6b), small particle like features (shown encircled) could be seen within the lightly etching grains, whose grain boundaries are mostly visible. In micrographs pertaining to 0.2 (Fig. 6c) and 0.5 °C/sec (Fig. 6d), the grain boundaries are not readily seen although traces of their presence can be seen at a few locations. At these cooling rates, many thick and dark etching parallel linear features (encircled) could be seen to populate the grain interiors. At 0.5 °C/sec, in addition to the dark etching linear features, fine linear lath like features could also be seen at a few locations on careful examination (shown encircled). They seem to start from

grain boundaries and increase in length till obstructed by another grain boundary. At 1 °C/sec and higher cooling rates, the discontinuously aligned dark features become difficult to distinguish clearly while the rest of the microstructure seems to get engulfed with increasing amounts of regions that etch relatively darker. The interior of these dark etching regions contain aligned dark and light etching regions (shown encircled) although their linear lengths are relatively short compared to that observed at 0.5 °C/sec. At cooling rates, above 1 °C/sec grain boundaries are extremely difficult to delineate and it becomes impossible at 50 °C/sec. Although subtle changes in microstructure with cooling rate could be observed in optical micrographs, it is difficult to categorically ascertain from optical micrographs as to what could have resulted in the marginal increase in hardness observed with increase in cooling rate. The minor variations in hardness on successive changes in cooling rate can, in general, be attributed to subtle changes in size of features: finer the feature, harder the material. Increase of cooling rate results in a refinement of the microstructure. SEM micrographs of two extreme cooling rates together with their corresponding optical micrographs at the same magnification of 1000x are shown in Fig. 7. No direct correlation could be derived from the details of the microstructural features captured in SEM and optical microscopy. Interpretation of SEM microstructures of this kind of steels is not straight forward as these secondary electron images also capture topology of the etched specimen together with microstructural features subjected to different contrast mechanisms at much higher resolution.

### 3.4 Possible Microstructural Constituents

As optical and SEM micrographs could not help in unambiguously identifying the microstructural features observed in the steel studied, a brief survey of microstructural constituents reported in the literature in this class of steels was carried out to list down probable and potential microstructural elements, summary of which is presented here. The same nomenclatures as used by the authors in their respective works are used here to describe the microstructural features. In HSLA 80/ASTM A710 steel, austenite transforms first to polygonal ferrite, and, subsequently, the remaining carbon-enriched austenite transforms to a variety of complex microconstituents depending on the cooling rate adopted (Ref 1). At cooling rates  $> 5$  °C/s, the transformation product mixture contains granular ferrite, acicular ferrite and martensite, all associated with films or islands of retained austenite. At cooling rates  $< 5$  °C/s, the mixture consists of lower bainite, upper bainite and martensite with retained austenite associated with martensite. In modified ASTM A710 HSLA steel, the dominant micro-constituent at a large range of intermediate cooling rates was granular bainite characterized by laths of ferrite and inter-lath particles of martensite and/or austenite (Ref 17). Fully martensitic microstructure was reported at cooling rates  $> 4$  °C/s on HSLA 100 steel with 0.04 and 0.06% C by Dhua et al.(Ref 14) and A D Wilson et al. (Ref 18), respectively. Between 0.4 and 4 °C/s, the microstructure was predominantly granular bainite and rest martensite. However at  $< 0.4$  °C/s, while the steel with 0.06%C revealed pro-eutectoid ferrite and granular bainite, the steel with 0.04%C did not reveal pro-eutectoid ferrite but revealed massive ferrite and granular bainite. A review of HSLA line pipe steels by NJ Kim (Ref 6) also pointed to presence of ferrite, bainite and martensite in similar steels. It is

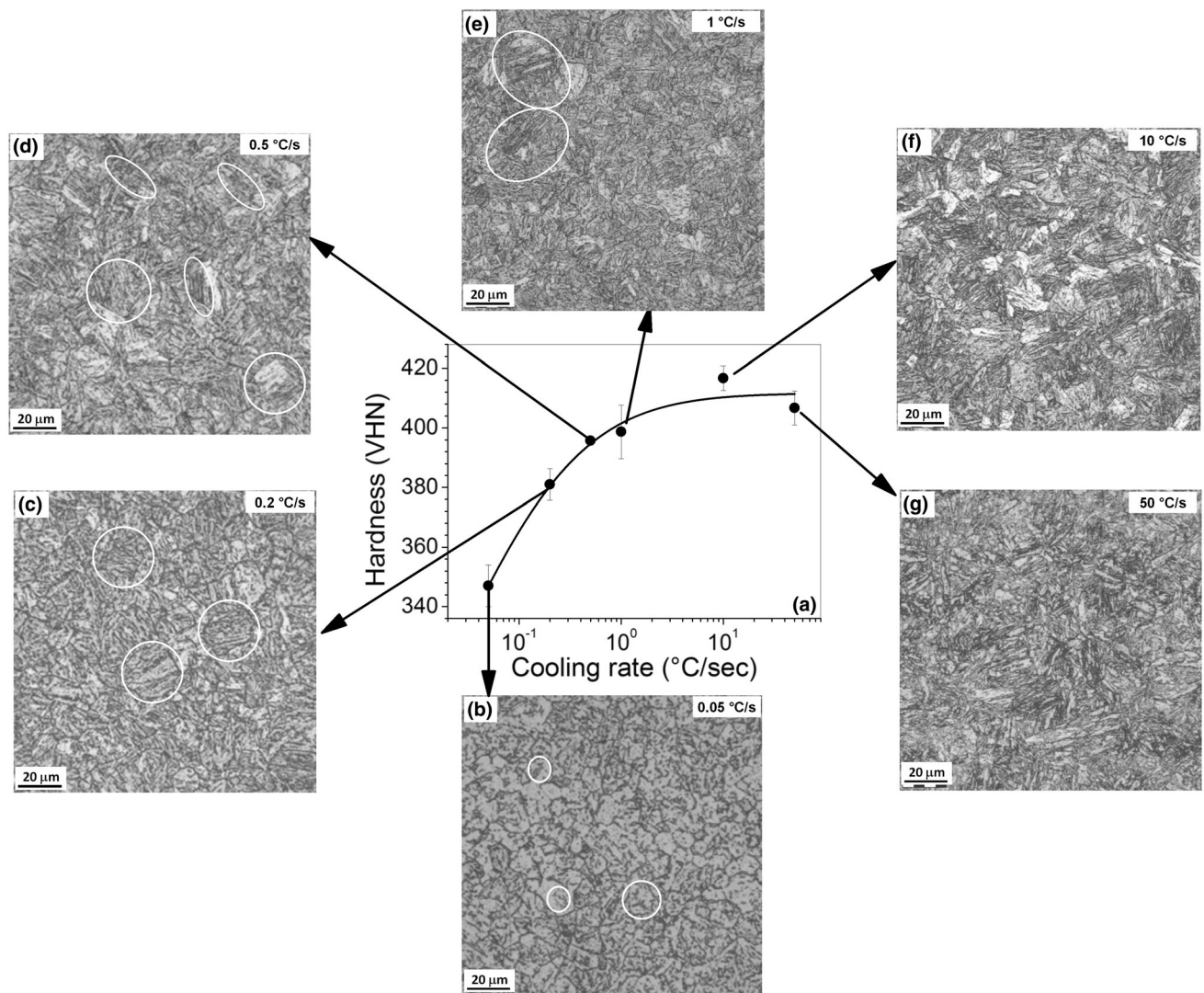


**Fig. 6** Optical micrographs of specimens corresponding to different cooling rates; shown here along with their hardness values

pertinent to note that in all the studies cited above, barring polygonal (Ref 1) and massive ferrite (Ref 14), which could be observed in optical microscope (Ref 14), identification and characterization of all other phases were carried out through transmission electron microscopy. On certain other Russian grade HSLA steels such as 09KhN2MD and 09KhN4MDFalso, the presence of a mixture of martensite and bainite has been reported, based on advanced analyses carried out using electron backscattering diffraction (Ref 12, 13). On the basis of these published findings, it can be expected that the transformation products in the HSLA steel being studied would also involve predominantly a mixture of martensite and bainite, relative fractions of which will be a function of cooling rate. However, to assess presence of other phases as well to differentiate and quantify the amount of bainite and martensite, advanced metallographic techniques will need to be resorted to (described in Sect. 3.5.2 (c)).

CCT diagrams of the above three HSLA steels were also reviewed to assess the sequence of microstructural evolution as a function of cooling rate. In HSLA 80 plate steel, initially a ferritic transformation (polygonal or Widmanstätten) and

subsequently a bainitic transformation takes place before martensitic transformation during cooling (Ref 1). It was seen that at cooling rates  $< 10$  °C/s, a mixture of upper and lower bainite forms at higher temperatures before martensite forms at lower temperatures. AD Wilson's work (Ref 18) on HSLA 100 plate steel revealed that while only martensite forms at higher cooling rates, the formation of granular bainite precedes the formation of martensite at lower cooling rates. In modified ASTM A710 HSLA steel, initial transformation to granular bainite over a large range of cooling rates was followed by martensitic transformation at lower temperatures (Ref 18). On the basis of these observations on similar HSLA steels, it can be summarized that decomposition of austenite involves the following transformations in the following order: 1. ferritic, 2. bainitic and 3. martensitic. While ferritic transformations happen at higher temperatures and martensitic transformations happen at lower temperatures, bainitic transformations occur at intermediate temperatures.

The CCT diagram generated in this study (Fig. 5) is examined in light of these observations. Among the four transformations represented in Fig. 5, martensitic transforma-

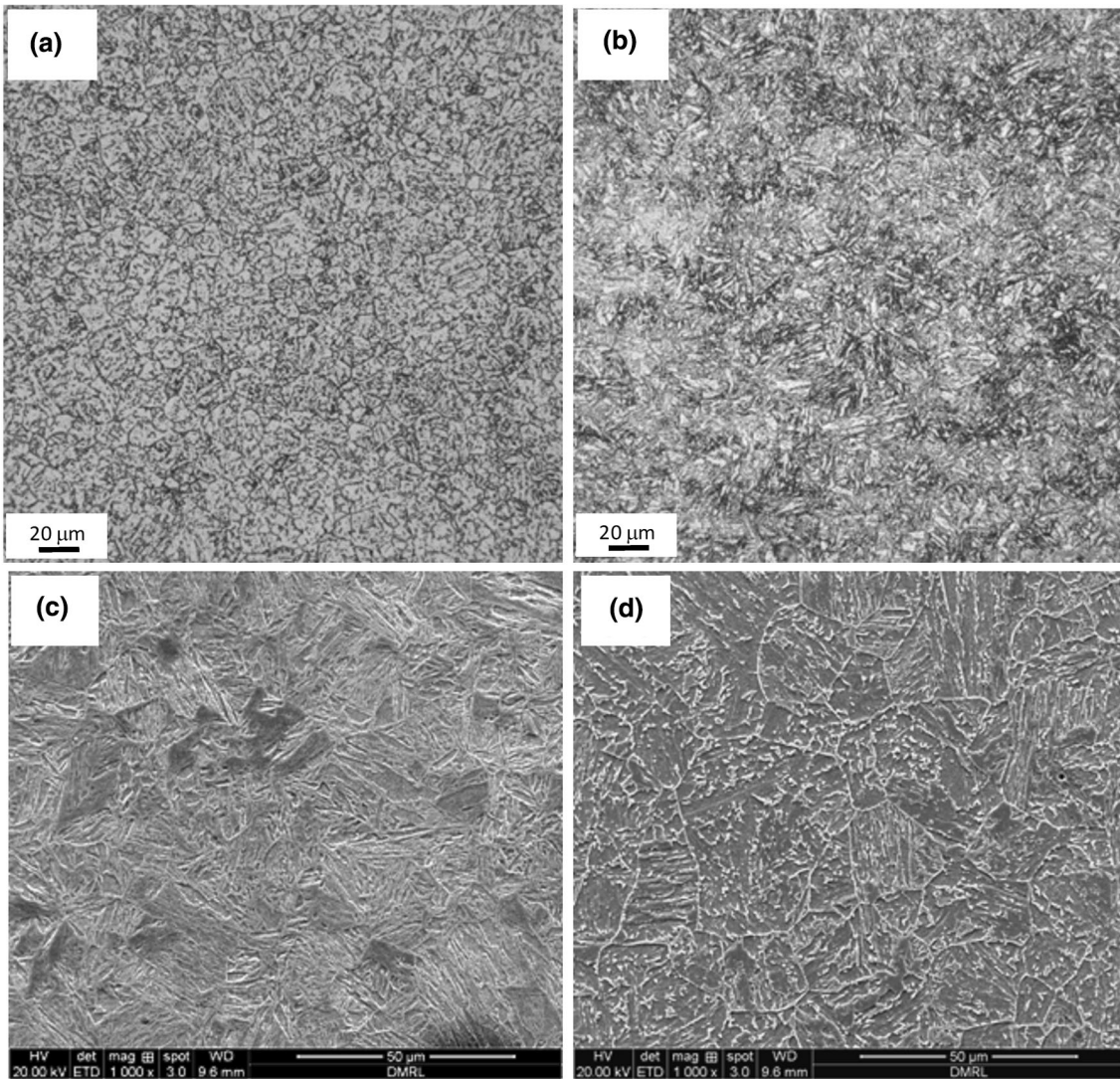


**Fig. 7** Optical & SEM micrographs of specimens cooled at 0.05 °C/sec (a),(c) and at 50 °C/sec (b),(d) at 1000 x magnification

tion is considered athermal (Ref 19) in nature. As athermal martensitic transformations do not need time to proceed and need only a sufficient thermodynamic driving force (that is obtained by significant undercooling below the critical temperature) (Ref 20), the temperature for start of martensitic transformation,  $M_s$ , does not typically vary with cooling rate. Following a refined empirical approach (Ref 21),  $M_s$  for the composition of the steel studied is estimated to be 345 °C. Combining these two aspects, the third transformation in Fig. 5 can be considered to correspond to martensitic start transformation. Since a bainitic transformation that precedes the martensitic transformation is expected as in other HSLA steels discussed above, the first and second transformations can be presumed to correspond to bainite start,  $B_s$  and bainite finish,  $B_f$  transformation points. This leads us to conclude that the fourth transformation corresponds to martensite finish,  $M_f$ , all of which are marked in Fig. 5. Details of microstructural studies carried out to confirm the above transformations are detailed in following Sections.

### 3.5 Quantitative Microstructural Characterization

During determination of the CCT diagram, the steel is taken into the austenitic region and then cooled at various rates down to 200 °C during which the austenite transforms, depending on the cooling rate, into various low-temperature microstructural constituents. These include ferrite (F), pearlite (P), bainite (B) and martensite (M). It is important to note that, among these, only F represents a pure phase in the thermodynamic sense; P, B and M (specifically when tempered martensite) are all essentially not pure phases, but are aggregates of ferrite and carbides (Ref 22), differing between each other in the mechanisms of nucleation and growth, which lead to differences in final microstructural features such as the size, morphology and orientation. For example, pearlite results from a diffusional transformation in which there is concurrent growth of ferrite and cementite in a lamellar form (Ref 23) and it can be distinguished without much difficulty, either using SEM or TEM. Similarly, depending on different evolution mechanisms that operate ferrite can also be present in different morphologies, viz., polygonal, massive, Widmanstätten, acicular, granular, etc. (Ref 24). However, often, as mentioned in the

previous section, it is not easy to distinguish between B, M and F in acicular morphology.

**3.5.1 Limitations of Optical Metallography.** Light optical metallography relies on differentiating microstructural constituents primarily with the help of their morphologies delineated by the metallographic etching process adopted. Both M (Ref 25) and B (Ref 26, 27) are known to exhibit lath morphology whose typical average lath width in this class of HSLA steel is about 500nm (Ref 14). B is known to etch darker (Ref 28) as they are associated with carbides: inter-lath carbides in upper B and intra-lath carbides in lower B. Similarly boundaries between variants of M laths, blocks and packets are also high-angle boundaries (Ref 29) like grain boundaries and as a result they too etch dark. Considering that M and B, both with similar lath morphology coexist within fine austenite grains whose boundaries also etch dark, differentiating them under an optical microscope is an arduous task even in the best of etched specimens. Retained austenite, whenever present, is typically in the form of very thin films and sometimes in the form of isolated small islands (Ref 1) in small quantities. These characteristics also render them difficult to identify from optical micrographs. While the general characteristics of the microstructure presented in Fig. 7 suggest the presence of B and/or M in the steel being studied, no quantitative information on its constituents could be ascertained from these optical micrographs for reasons explained above. Such difficulties in microstructural characterization of complex constituents in steels through optical metallography are rather well known and documented (Ref 30, 31). Similar challenges exist with conventional SEM investigations as well. However, from the optical micrographs at Fig. 7, it is clear that featureless and light etching polygonal ferrite (Ref 1) and massive ferrite (Ref 14) seen in certain other HSLA steels are obviously not present in the steel studied (Fig. 7). Thus, we can safely conclude that the primary matrix constituents in the present case are M and B, the distinction and quantification of which needs other techniques. While transmission electron microscopy (TEM) studies can shed light on crystallographic and morphological aspects of phases in the microstructure, only a limited area is analyzed and hence quantification of the relative volume fractions of the different matrix microstructural constituents can be only indicative in the best of circumstances and downright misleading at times. Hence, quantification of relative fractions of B and M in steels, especially low-alloy low-carbon steels such as the one presently under study, has always been a challenge. However, in recent times, advanced techniques based on electron backscatter diffraction (EBSD)-based analyses have been shown to be remarkably successful in providing reliable estimates of the relative fractions of the matrix microstructural constituents in these steels (Ref 12, 13). Our attempts of using these techniques to understand the microstructures that result from the different cooling rates in the present study are described in the following section.

**3.5.2 Electron Backscatter Diffraction Analysis.** EBSD is a powerful technique, usually employed in conjunction with SEM, and gives crystallographic information about the microstructure at length scales ranging from tens of nanometers to several hundred micrometers. EBSD can be quite effectively employed in steels when seeking to separate austenite (which has the FCC crystal structure) from the transformed low-temperature phases such as F, B or M, which are predominantly BCC in nature (Ref 32-34). While M is strictly BCT, in low-

carbon steels, the tetragonality is too small to be discernible in EBSD, and thus all the low-temperature constituents index as BCC. It is therefore non-trivial to distinguish between F, B and M (Ref 30) using EBSD techniques. It is especially difficult to distinguish B and M.

Several strategies have been employed to attempt to distinguish between the phases indexed as BCC in EBSD analyses. All these rely on post-processing of the EBSD data (Ref 35, 36) and exploit information such as image quality, confidence index, kernel average misorientation (KAM) or grain average misorientation (which is KAM, but within a single parent grain). Of these, KAM and GAM have been found to be very effective for low-carbon low-alloy steels. As the focus in this study is to differentiate and quantify B and M, primarily of lath morphology, the width of the lath was considered as an important parameter while finalizing the scan step size such that at least five scan points across a typical lath are ensured for adequate data collection. Therefore, in our case after conducting several trials, the EBSD scan conditions were carefully chosen keeping a balance between scan step size (scan-resolution) and the magnification to meet the objective of identification and quantification of B and M constituents. All the specimens were scanned at an optimized magnification of 2500 $\times$  and a step size of 0.225  $\mu\text{m}$ .

**3.5.2.1 High- and Low-Angle Boundaries.** As an example, the typical results from the basic EBSD data for the specimen cooled at 0.05  $^{\circ}\text{C}/\text{sec}$  are shown in Fig. 8. The band contrast (BC) is a measure of the quality of the Kikuchi pattern obtained from each pixel, and therefore, it often reveals boundaries that are sometimes not visible even in an electron image Fig. 8(a). It must be noted that the pattern quality, & hence the BC image, is also affected by things such as residual strain and sample preparation. Nevertheless, other things being equal, the BC image can be used to obtain at least a semi-quantitative understanding of the nature of the boundaries in the microstructure. Figure 8(b) shows the BC image with an overlay of the detected boundaries, delineated by the limits given in Fig. 8(c). It can be seen from the frequency histogram of boundaries (Fig. 8(c)) that there is a negligible number of boundaries in the 20-40 $^{\circ}$  range. This is observed for all the samples investigated in this study, and is a characteristic feature of mixed B/M microstructures with negligible amount of other phases such as untransformed austenite or polygonal ferrite (Ref 25, 27, 29). The low-angle boundaries (2-20 $^{\circ}$ ) exist essentially between different lath packets, while the high-angle grain boundaries (40-65 $^{\circ}$ ) could be either due to prior austenite grain boundaries, or due to different variants of B/M. Figure 8(d) is an inverse pole figure (IPF) image with an overlay of the high-angle boundaries. It is, however, clear that none of these images typically generated through EBSD can help in identifying whether the microstructural constituent in a particular location is B or M.

**3.5.2.2 Grain Average Misorientation.** As standard EBSD analyses cannot help in distinguishing F, B and M, approaches based on dislocation densities have gained importance as F, B and M have different dislocation densities (Ref 37). In order to distinguish them from one another, a technique is required that can measure the changes driven by the change in dislocation densities. It is well established in the literature that the lattice distortion (i.e., departure of atomic position from an ideal structure) is associated with the presence of dislocations. The extent of lattice distortion depends on density of dislocations which cause lattice curvature (Ref 38, 39) and is also referred as



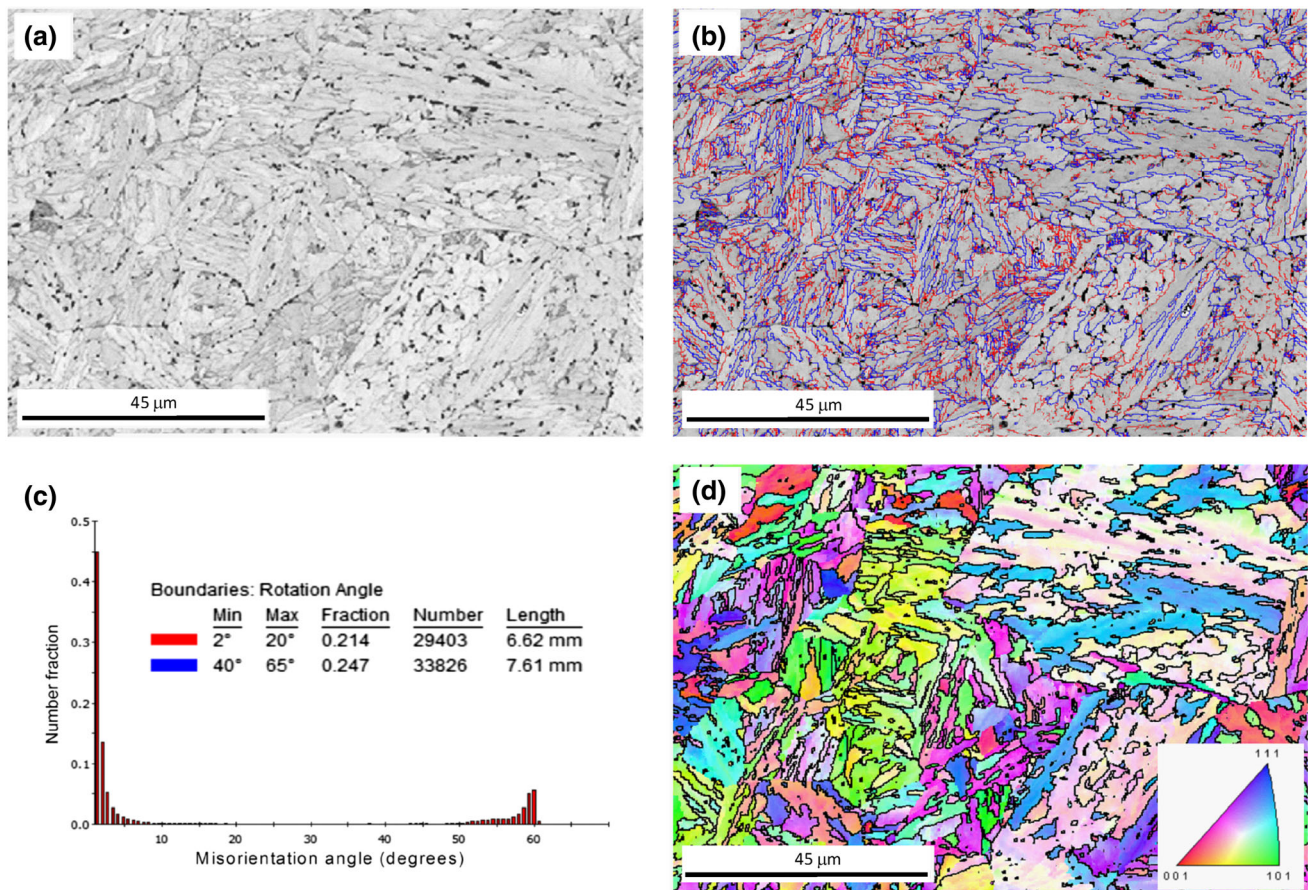


**Fig. 8** (a) Band contrast image; (b) band contrast image with high and low-angle boundary overlay (red line: 2°-20°; blue line: 45°-65°); (c) distribution of number fraction of misorientation with misorientation angle; (d) IPF image at cooling rate 0.05 °C/sec. All images were captured at 2500× magnification and step size 0.225

**Table 2** Thresholds for misorientation spread (\*Misorientation spread for various microstructural constituents were adopted based on Zisman's approach (Ref 12, 13))

Misorientation spread*, Δ	Microstructural constituent	Remarks
$0 < \Delta < 0.40^\circ$	Ferrite	Lowest dislocation density among BCC phases
$0.40 < \Delta < 0.55^\circ$	Bainite (B-I)	Dislocation density closest to that of ferrite
$0.55 < \Delta < 0.70^\circ$	Bainite (B-II)	Intermediate dislocation density
$0.70 < \Delta < 0.85^\circ$	Bainite (B-III)	Dislocation density close to that of martensite
$0.85 < \Delta < 5.00^\circ$	Martensite	Highest dislocation density

crystal curvature (Ref 40). Though the crystal curvature cannot be directly deduced from the data obtained from conventional EBSD (which gives information about only the crystallographic orientation), however, the orientation differences between the neighboring points in the map obtained from orientation imaging microscopy using EBSD are analogous to the crystal curvature. The lattice distortion due to different density of dislocations in F, B and M manifests itself as different lattice curvature in F, B and M, and can therefore be quantified by the use of suitable parameter such as angular misorientation between neighboring points (Ref 41, 42). Such changes are captured by using either of two approaches that deal with distribution of local crystallographic orientation viz., kernel average misorientation (KAM) and grain average misorienta-

tion (GAM) (Ref 34, 43, 44). KAM is the averaged misorientation angle that a pixel makes with the surrounding neighbor pixels, and is useful for indicating the local lattice curvature (Ref 45). GAM is a similar function that can be derived in the grain scale by averaging the intra-granular misorientation angles between the neighboring pixels. This grain average misorientation (GAM) is useful for characterizing the accumulation and localization of plastic strain (Ref 46). GAM can in principle be regarded as the grain average of KAM. The GAM function is a standard option of the TSL OIM analysis software. In this work, we have exploited GAM-based analysis to identify and also quantify fractions of F, B and M.

In order to distinguish F, B and M in the microstructure using a GAM-based technique, it is necessary to identify the

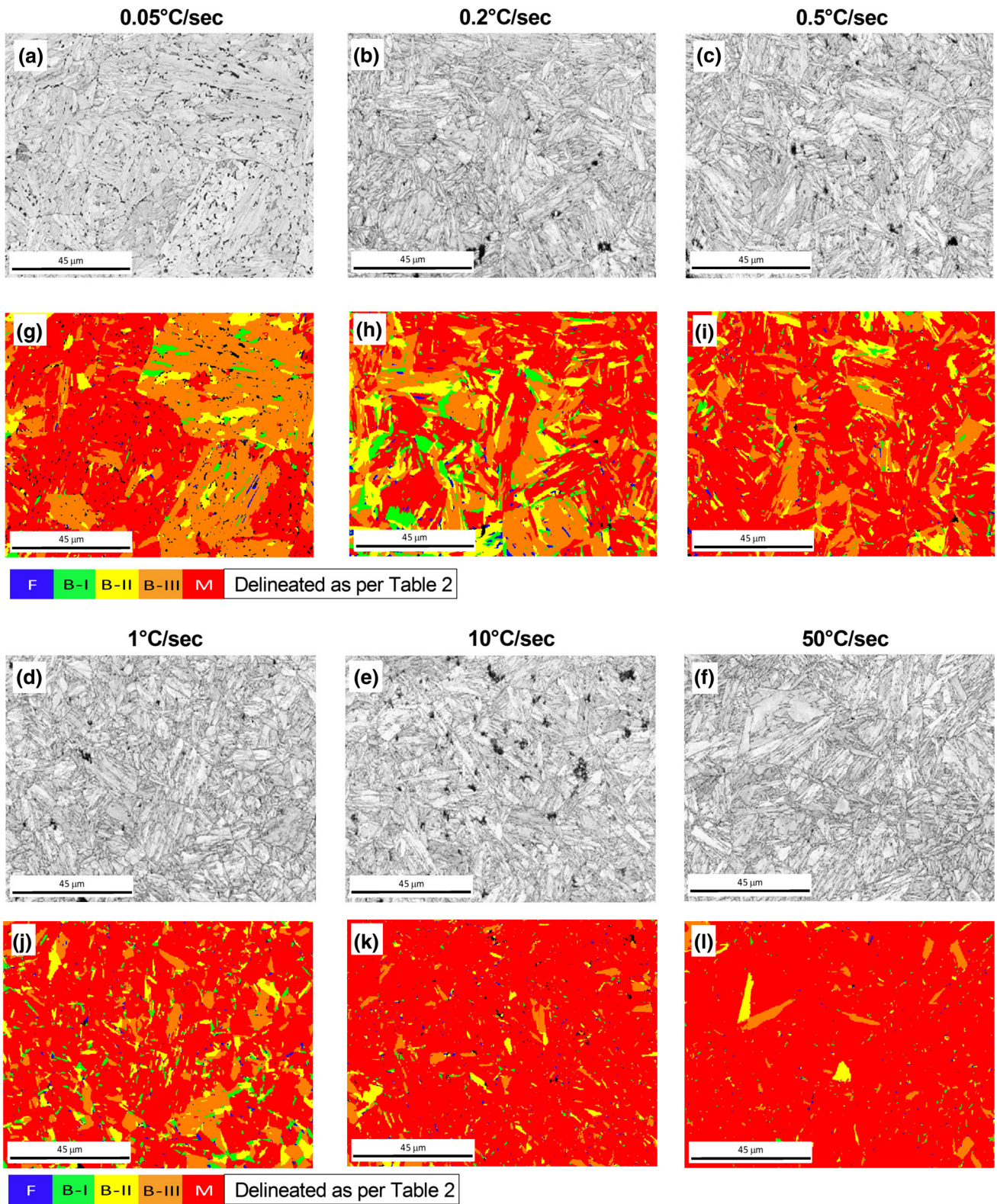


**Fig. 9** Band contrast images with corresponding GAM images for different cooling rates recorded at 2500X magnification and step size 0.225 (a),(g) for 0.05 °C/sec (b),(h) for 0.2 °C/sec (c),(i) for 0.5 °C/sec. Band contrast images with corresponding GAM images for different cooling rates recorded at 2500X magnification and step size 0.225 (d),(j) for 1 °C/sec (e),(k) for 10 °C/sec (f),(l) for 50 °C/sec

corresponding thresholds for the chosen parameter, in this case, the grain average misorientation spread,  $\Delta$ . In the present work, we have adopted the thresholds employed by Zisman et al. (Ref 12, 13), as the steel in the present study is of the same class and

similar to the one studied by those researchers. Following Zisman’s approach, the microstructural constituents were divided into five categories based on the misorientation spread as indicated in Table 2. The band contrast images of the

**Table 3** Low and high angle boundary lengths as a function of cooling rate

Cooling Rate (°C/sec)	Length of LAGB, mm (2°-20°)	Length of HAGB, mm (40°-65°)	Total length (mm) LAGB+HAGB	% LAGB	% HAGB	% increase in total length relative to 0.05 °C/sec
0.05	6.62	7.61	14.23	46.5	53.5	0
0.2	7.69	9.90	17.59	43.7	56.3	23.6
0.5	10.10	9.19	19.29	52.4	47.6	35.6
1	10.30	8.27	18.57	55.5	44.5	30.5
10	14.30	7.59	21.89	65.3	34.7	53.8
50	16.10	7.74	23.84	67.5	32.5	67.5

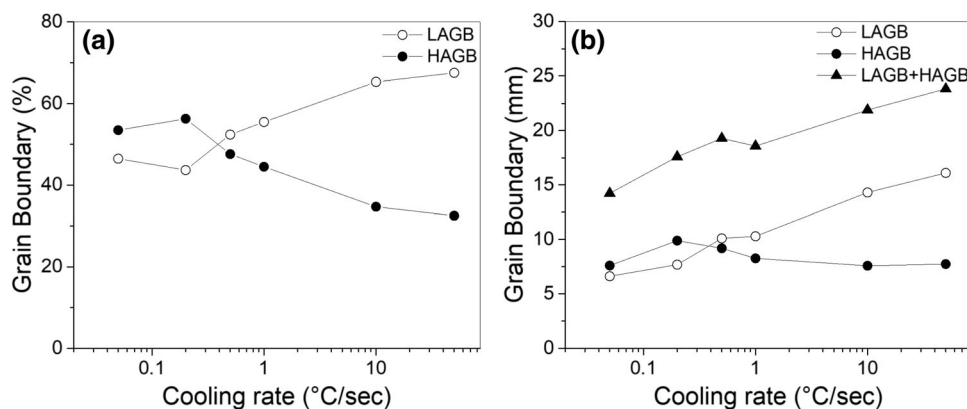


**Fig. 10** (a) Change of grain boundary (LAGB & HAGB) percentage in specimens cooled at different cooling rates, (b) variation of low-angle, high-angle and total boundary length with cooling rate

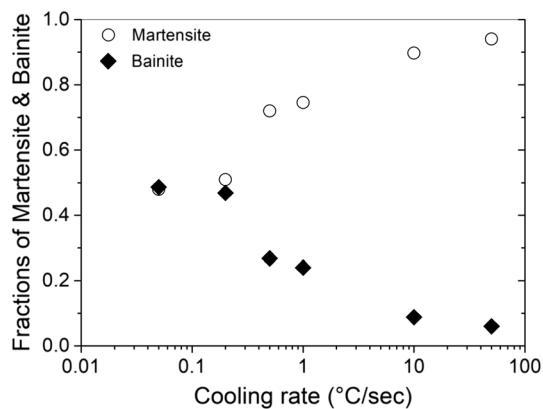


**Fig. 11** Change of fractions of martensitic and bainitic (calculated by combining three types bainite; B-I, B-II and B-III) as a function of specimen cooling rates

samples cooled at different cooling rates ranging from 0.05 to 50 °C/s are shown in Fig. 9(a)-(f). The corresponding GAM images are shown in Fig. 9(g)-(l) with color scale as per Table 2. The ability of GAM to differentiate B from M is immediately clear. The band contrast image in Fig. 9(a) is able to show the different boundaries, but it is not apparent as to which regions are B and which ones are M. However, through the corresponding GAM image segmented with thresholds suggested by Zisman (Fig. 9(g)), it is now possible to visually distinguish B and M. It can also be seen easily that the content of M progressively increases (Fig. 9(g)-(l)) with increase in

cooling rate (48% at 0.05 °C/s to 94% at 50 °C/s). Considering the fraction of B and M in specimens cooled at different cooling rates and the way B and M are distributed in the microstructure (evident from Fig. 9(g)-(l)), it is obvious that this EBSD-based approach is far more powerful in identifying and quantifying B and M contents as it samples much larger areas that that would be possible through TEM. Another aspect evident from figures in Fig. 9(b)-(f) is that the overall structure gets finer, i.e., more number/length of boundaries with increase in cooling rate. In order to understand quantitatively the increasing fineness of the structure, we can make use of the boundary length information shown textually in the plots of misorientation angle distribution (Example: Fig. 9(c)). Boundary length data compiled for all the cooling rates is shown in Table 3 and plotted as Fig. 10 for easy reference. It can be seen that the overall boundary length increases 67% on going from a cooling rate of 0.05 °C/s to 50 °C/s. Closer analysis reveals that the increase is largely due to the increase in the length of low-angle grain boundaries (2-20°), from 46.5% of the total for 0.05 °C/s to 67.5% of the total for 50 °C/s.

**3.5.2.3 Quantification of Bainite and Martensite Area Fraction.** As our primary interest is to look at relative fractions of B and M, the overall B content at a given cooling rate was determined by summing up the fractions of B-I, B-II and B-III. The volume fraction of M and B determined as a function of cooling rate is shown in Fig. 11. With increase in cooling rate, the content of M is seen to increase together with a reduction in content of B. While B content reduced with increase in cooling rate (~49% at 0.05 °C/s to 6% at 50 °C/s), even at the highest cooling rate studied, i.e., 50 °C/s, B could not be fully avoided

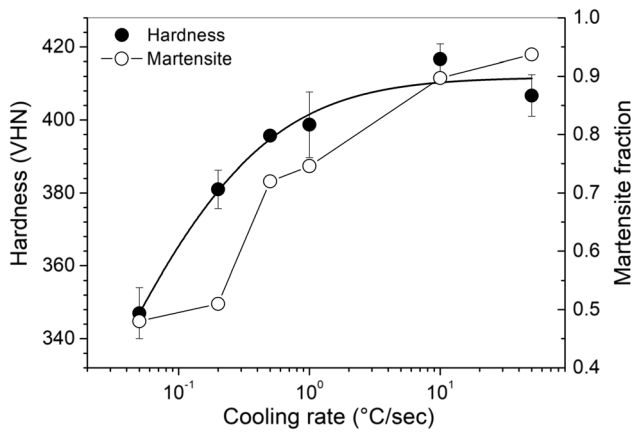


**Fig. 12** Trend in variation of hardness and martensite fraction for specimens cooled at different cooling rates

(~94% M and 6% B). Volume fraction of B-III, which is more closer to martensite in terms of dislocation density, is seen to be higher at all cooling rates compared to B-I and B-II (Figs. 9g-l). At no cooling rate did ferrite fraction exceed 1.2%, which is quite consistent with the observations made through optical microscopy. Identification of B and M described in the previous section and its quantification described here are experimental validation and confirmation of  $B_s$ ,  $B_f$ ,  $M_s$  and  $M_f$  temperatures, which were, to start with, assigned and marked in Fig. 5 on the basis of estimated  $M_s$  temperature and logical reasoning built on observations on other similar steels.

**3.5.3 Microstructural Correlation with Hardness.** Having identified and quantified M and B constituents of the microstructure as a function of cooling rate (as discussed in Sect. 3.5.2 (b) and 3.5.2 (c) above), its correlation to overall hardness is understood by plotting both hardness and volume fraction of M against cooling rate as shown in Fig. 12. It is evident that the increase in hardness with cooling rate correlates very closely with the associated increase in M content. As hardness of M is known to be higher than that of B for any given carbon content (Ref 28) (p. 304), owing primarily to high carbon super-saturation and high dislocation density associated with displacive transformation through which M forms, the increase in hardness with increasing martensite content is on expected lines.

## 4. Conclusions

Austenite decomposition during cooling of an indigenously developed Cu-bearing HSLA steel has been studied through systematic dilatometry experiments carried out at cooling rates ranging over three orders of magnitude (0.05-50 °C/s). Key outcomes from the work are:

- During cooling, across all the cooling rates explored in the study, austenite is seen to transform predominantly to a mixture of martensite and bainite.
- An EBSD-based methodology utilizing GAM as a tool could be employed to differentiate martensite from bainite and quantify their volume fractions.
- Martensite content increases and bainite content decreases with increase in cooling rate. While martensite content in-

creased from 48 to 94% with increase in cooling rate from 0.05 to 50 °C/s, bainite content decreased from 49 to 6% over the same cooling rate.

- Microstructural observations correlate well with the increase in hardness observed with increase in cooling rate.
- CCT diagram for the steel has been constructed through careful analyses of the dilatograms together with advanced EBSD analyses of microstructure and correlations with hardness measurements.
- The present work provides an understanding of the microstructural constituents of the steel as a function of cooling rate imposed. Alternately, from the hardness measured, one can estimate the microstructural constituents and the cooling rate imposed. These findings will prove useful for resolving problems when desired properties are not met in the product after industrial heat treatment. Further, through a correlation between the hardness and other mechanical properties such as strength and sub-zero impact toughness (which have not been investigated in the current study), the results from this study can be used to identify the minimum cooling rate that would be necessary to achieve desired mechanical properties in the final product during industrial production.

## Acknowledgment

The authors would like to thank Director, DMRL, for providing continuous support and encouragement for carrying out this work.

## References

1. S.W. Thompson, D.J. Colvin, and G. Krauss, Austenite Decomposition During Continuous Cooling of an HSLA-80 Plate Steel, *Metall. and Mater. Trans. A.*, 1996, **27**, p 1557–1571.
2. J.R. Davis, High-Strength Low-Alloy Steels, Alloying: Understanding the Basics, 1st ed., ASM International, 2001, p 193-209
3. S.Vervynck, K. Verbeken., B. Lopez, and J.J. Jonas, Modern HSLA steels and role of non-recrystallisation temperature, *International Materials Reviews*, 2012, **57**(4), p 187-207
4. The greatest depth of immersion of submarines of the Russian Navy, US Navy and Japan, <https://weaponews.com/weapons/65355810-the-greatest-depth-of-immersion-of-submarines-of-the-russian-navy-us-n.html>, Accessed on 24 June 2021
5. A. Danijel, Skobir, Visokotrdna Malolegirana (HSLA) Konstrukcijskajekla (High-Strength Low-Alloy (Hsla) Steels), *Materiali in Tehnologije*, 2011, **45**(4), p 295–301.
6. N.J. Kim, The Physical Metallurgy of HSLA Linepipe Steels- A Review, *J. Metals*, 1983, **35**(4), p 21–27.
7. Ernest J. Czyryca, Richard E. Link, Richard J. Wong, Denise A. Aylor, Thomas W. Montemarano, and John P. Gudas, Development and Certification of HSLA -100 Steel for Naval Ship Construction, *Naval Engineers Journal*, 1990, **63**, 102(3)
8. G. Malkondaiah, M. Srinivas, and R. Balamuralikrishnan, High performance steels for Indian defence, *IIM Metal News*, 2012, **15**(2), p 28–31.
9. Nirmalya Rarhi, Parmanand Bairwa, R. Veerababu, K. Ankalu, S. Nagarjuna, R. Balamuralikrishnan, K. Muraleedharan, and M. Srinivas, Development of 780 MPa Steels for Naval Applications: Part-I: Initial Trials on Composition and Heat Treatment Optimization, DRDO-DMRL-SSG-33, DMRL Technical Report, DMRL, India, 2012
10. Nirmalya Rarhi, Paramanand Bairwa, K. Ankalu, R. Balamuralikrishnan, S. Nagarjuna, K. Muraleedharan, and M. Srinivas, Development of 780 MPa Steels for Naval Applications: Part-II: Composition Refinement and Establishment of Reproducibility, DRDO-DMRL-SSG-068, DMRL Technical Report, DMRL, India, 2014

11. G.K. Prior, The role of dilatometry in the characterisation of steels, *Mater. Forum*, 1994, **18**, p 265–276.
12. A.A. Zisman, S.N. Petrov, and A.V. Ptashnik, Quantitative Verification of High-Strength Alloyed Steel Bainite-Martensite Structures by Scanning Electron Microscopy Methods, *Metallurgist*, 2015, **58**(11–12), p 1019–1024. (in Russian)
13. A. A. Zisman, N. Yu. Zolotarevsky, S. N. Petrov, E. I. Khlusova, and E. A. Yashina, Panoramic Crystallographic Analysis of Structure Evolution in Low-Carbon Martensitic Steel under Tempering Metal Science and Heat Treatment, 2018, **60** (3–4), p 142–149, in Russian
14. S.K. Dhua, D. Mukerjee, and D.S. Sarma, Effect of cooling rate on the as-quenched microstructure and mechanical properties of HSLA-100 steel plates, *Metall. and Mater. Trans. A.*, 2003, **34**, p 2493–2504.
15. S.W. Thompson, D.J. Colvin and G. Krauss, Continuous cooling transformations and microstructures in a low-carbon, high-strength low-alloy plate steel, *Metall. Trans. A.*, 1990, **21**, p 1493–1507.
16. Y-J Yang, J-X Fu, R-J Zhao, and Y-X Wu, Dilatometric Analysis of Phase Fractions During Austenite Decomposition in Pipeline Steel, 3rd International Conference on Material, Mechanical and Manufacturing Engineering (IC3ME2015), Prasad Yarlagadda, June 27–28, 2015, Guangzhou, China, p 2186–2190
17. S.W. Thompson, D.J. Colvin, and G. Krauss, On the bainitic structure formed in a modified A710 steel, *Scripta Metall.*, 1988, **22**(7), p 1069–1074.
18. A.D. Wilson, E.G. Hamburg, D.J. Colvin, S.W. Thompson, and G. Krauss, Proc. Int. Conf. on Microalloyed HSLA Steel, Microalloying'88, ASM International, Metals Park, OH, 1988, p 259–275
19. Harry Bhadeshia, and Robert Honeycombe, Formation of Martensite, Steels: Microstructure and Properties, 3rd ed., Butterworth-Heinemann, 2006, p 95
20. D.E. Laughlin, N.J. Jones, A.J. Schwartz, and T.B. Massalski, Thermally Activated Martensite: Its Relationship to Non-Thermally Activated (Athermal) Martensite, G. B. Olson, D. S. Lieberman, and A. Saxena, (Ed.) International Conference on Martensitic Transformations (ICOMAT), New Mexico, 2010, p 141–144
21. C. Capedevila, F.G. Caballero, and C. Garcia de Andres, Determination of Ms Temperature in Steels: A Bayesian Neural Network Model, *ISIJ Int.*, 2002, **42**, p 894–902.
22. R. Abbaschian, L. Abbaschian, and R.E. ReedHill, The transformation of austenite to Pearlite, Physical Metallurgy Principles, 4th ed., Cengage Learning, 2009, p 568
23. S.-W. Seo, H.K.D.H. Bhadeshia, and D.W. Suh, Pearlite growth rate in Fe-C and Fe-Mn-C Steels, *Mater. Sci. Technol.*, 2015, **31**, p 487–493.
24. G. Krauss and S.W. Thompson, Ferritic Microstructures in Continuously Cooled Low- and Ultralow-carbon Steels, *ISIJ Int.*, 1995, **35**(8), p 937–945.
25. S. Morito, X. Huang, T. Furuhashi, T. Maki, and N. Hansen, The Morphology and Crystallography of Lath Martensite in Alloy Steels, *Acta Mater.*, 2006, **54**(19), p 5323–5331.
26. B.L. Bramfitt and J.G. Speer, A Perspective on the Morphology of Bainite, *Metall. Trans. A.*, 1990, **21**(3), p 817–829.
27. S. Zajac, V. Schwinn, and K.H. Tacke, Characterisation and Quantification of Complex Bainitic Microstructures in High and Ultra-High Strength Linepipe Steels, *Mater. Sci. Forum*, 2005, **500–501**, p 387–394.
28. H.K.D.H. Bhadeshia, *The Discovery of Bainite, Bainite in Steels: Theory and Practice*, 3rd ed. CRC Press, Boca raton, 2015, p 2
29. H. Kitahara, R. Ueji, N. Tsuji, and Y. Minamino, Crystallographic Features of Lath Martensite in Low-Carbon Steel, *Acta Mater.*, 2006, **54**, p 1279–1288.
30. S.-H. Na, J.-B. Seol, M. Jafari, and C.-G. Park, A Correlative Approach for Identifying Complex Phases by Electron Backscatter Diffraction and Transmission Electron Microscopy, *Appl. Microsc.*, 2017, **47**(1), p 43–49.
31. K.-S. Min-SeokBaek, T.-W. Park, J. Ham, and K.-A. Lee, Quantitative Phase Analysis of Martensite-Bainite Steel Using EBSD and its Microstructure, Tensile and High-Cycle Fatigue Behaviors, *Mater. Sci. Eng., A*, 2020, **785**(139375), p 1–13.
32. C. Herrera, D. Ponge, and D. Raabe, Design of a Novel Mn-Based 1 GPa Duplex Stainless TRIP Steel with 60% Ductility by a Reduction of Austenite Stability, *Acta Mater.*, 2011, **59**, p 4653–4664.
33. R. Petrov, L. Kestens, A. Wasilkowska, and Y. Houbaert, Microstructure and Texture of a Lightly Deformed TRIP-Assisted Steel Characterized by Means of the EBSD Technique, *Mater. Sci. Eng. A*, 2007, **447**(1–2), p 285–297.
34. S. Zaefferer, J. Ohlert, and W. Bleck, A Study of Microstructure, Transformation Mechanisms and Correlation Between Microstructure and Mechanical Properties of a Low Alloyed TRIP Steel, *Acta Mater.*, 2004, **52**, p 2765–2778.
35. O. Man, L. Pantělejev, and Z. Pešina, EBSD Analysis of Phase Compositions of Trip Steel on Various Strain Levels, *Mater. Eng.*, 2009, **16**, p 15–21.
36. A.A. Gazder, F. Al-Harbi, H. ThSpanke, and D.R.G. Mitchell, A Correlative Approach to Segmenting Phases and Ferrite Morphologies in Transformation-Induced Plasticity Steel Using Electron Back-Scattering Diffraction and Energy Dispersive X-ray Spectroscopy, *Ultramicroscopy*, 2014, **147**, p 114–132.
37. M. Takahashi and H.K.D.H. Bhadeshia, Model for Transition from Upper to Lower Bainite, *Mater. Sci. Technol.*, 1990, **6**(7), p 592–603.
38. J.F. Nye, Some Geometrical Relations in Dislocated Crystals, *Acta Metall.*, 1953, **1**(2), p 153–162.
39. F. Sozio and A. Yavari, On Nye's Lattice Curvature Tensor, *Mech. Res. Commun.*, 2021, **113**, p 103696.
40. A.A. Zisman, Choice of Scalar Measure for Crystal Curvature to Image Dislocation Substructure in Terms of Discrete Orientation Data, *J. Mech. Behr. Mater.*, 2016, **25**(1–2), p 15–22.
41. W. Pantleon, Resolving the Geometrically Necessary Dislocation Content by Conventional Electron Backscattering Diffraction, *Scripta Mater.*, 2008, **58**, p 994–997.
42. O. Muránsky, L. Balogh, M. Tran, C.J. Hamelin, J.-S. Park, and M.R. Daymond, On the Measurement of Dislocations and Dislocation Substructures Using EBSD and HRSD Techniques, *Acta Mater.*, 2019, **175**, p 297–313.
43. J.-Y. Kang, Do Hyun Kim, Sung-II Baik, Tae-Hong Ahn, Young-Woon Kim, Heung Nam Han, Kyu Hwan Oh, Hu-Chul Lee, Seong Ho Han, Phase Analysis of Steels by Grain-averaged EBSD Functions, *ISIJ Int.*, 2011, **51**(1), p 130–136.
44. Y. Wang and L. Li, Microstructure Evolution of Fine Grained Heat Affected Zone in Type IV Failure of P91 Welds, *Weld. Res.*, 2016, **95**, p 27–36.
45. S. Zaefferer, P. Romano, and F. Friedel, EBSD as a Tool to Identify and Quantify bainite and Ferrite in Low-Alloyed Al-TRIP Steels, *J. Microsc.*, 2008, **230**(3), p 499–508.
46. J.-Y. Kang, B. Bacroix, H. Regle, K.H. Oh, and H.-C. Lee, Effect of Deformation Mode and Grain Orientation on Misorientation Development in a Body-Centered Cubic Steel, *Acta Mater.*, 2007, **55**, p 4935–4946.

**Publisher's Note** Springer Nature remains neutral with regard to jurisdictional claims in published maps and institutional affiliations.